



ELSEVIER

Contents lists available at SciVerse ScienceDirect

Earth and Planetary Science Letters

journal homepage: www.elsevier.com/locate/epsl

Rolling hills on the core–mantle boundary

 Daoyuan Sun^{a,*}, Don V. Helmberger^b, Jennifer M. Jackson^b, Robert W. Clayton^b, Dan J. Bower^b
^a Department of Terrestrial Magnetism, Carnegie Institution of Washington, 5241 Broad Branch Road, NW, Washington, DC 20015, USA

^b Seismological Laboratory, California Institute of Technology, 1200 E. California Blvd., MS 252-21, Pasadena, CA 91125, USA

ARTICLE INFO

Article history:

Received 14 June 2012

Received in revised form

6 October 2012

Accepted 30 October 2012

Editor: P. Shearer

Available online 11 December 2012

Keywords:

core–mantle boundary (CMB)

iron-rich (Mg,Fe)O

USArray

low velocity zone

ABSTRACT

Recent results suggest that an iron-rich oxide may have fractionally crystallized from a primordial magma ocean and settled on the core–mantle boundary (CMB). Based on experimental results, the presence of only a few percent of Fe-rich oxide could slow seismic waves down by several percent. This heavy layer can become highly undulating as predicted from dynamic modeling but can remain as a distinct structure with uniform velocity reductions. Here, we use the large USArray seismic network to search for such structures. Strong constraints on D'' are provided by the core-phase SKS where it bifurcates, containing a short segment of P -wave diffractions (P_d) when crossing the CMB, called SKS_{*d*}. Synthetics from models with moderate velocity drops (less than 10%) involving a layer with variable thickness, perhaps a composite of sharp small structures, with strong variation in thickness can explain both the observed SKS_{*d*} waveforms and large scatter in differential times between SKKS and SKS. A smooth 3D image is obtained from inverting SKS_{*d*} waveforms displaying rolling-hills with elongated dome-like structures sitting on the CMB. The most prominent one has an 80-km height, $\sim 8^\circ$ length, and $\sim 4^\circ$ width, thus adding still more structural complexity to the lower mantle. We suggest that these results can be explained by a dynamically-stabilized material containing small amounts ($\sim 5\%$) iron-rich (Mg,Fe)O providing a self-consistent physical interpretation.

© 2012 Elsevier B.V. All rights reserved.

1. Introduction

The lowermost mantle region (D'') has been known by seismologists to be complex for over 50 yr (Helmberger et al., 2005; Jeffreys, 1962; Lay and Garnero, 2011; Sidorin et al., 1999), but only recently have mineral-physicists provided evidence for possible explanations: phase changes of perovskite (Hirose, 2006; Mao et al., 2006, 2004; Mosenfelder et al., 2007; Murakami et al., 2004; Oganov and Ono, 2004), iron-enriched oxides (Knittle and Jeanloz, 1991), and possible melt-accumulation (Hernlund and Tackley, 2007; Labrosse et al., 2007). Each of these physical states uniquely impacts dynamic models involving heat transfer from the core to mantle (Hernlund and Tackley, 2007; Lay et al., 2008; van der Hilst et al., 2007). Thus, extended length-scale images of P and S velocities will provide key information in developing compatible thermo-chemical dynamic models for the core–mantle boundary region.

A review of the multi-disciplinary evidence of lowermost mantle structure indicates discrete regions containing the D'' , possibly related to perovskite to post-perovskite (Pv–PPv) transition (Fig. 1A), and Large Low Shear Velocity Provinces (LLSVPs), where most of the ultralow-velocity zones (ULVZs) occur near the edges (McNamara et al., 2010). There are some rather isolated ULVZ's such as those reported beneath Iceland (Helmberger et al., 1998) and mid-Pacific (Mori and Helmberger, 1995). In most cases, it is difficult to obtain the 3D structure of ULVZ's. There are other regions more PREM-like, although there may be a thermal-boundary layer to accommodate a back transformation of PPv to Pv (Hernlund et al., 2005) (Fig. 1B).

The complexity of D'' could be caused by heterogeneity involving a mixture of iron-rich oxides and silicates (Knittle and Jeanloz, 1991; Wicks et al., 2010). Some recent constraints on heterogeneity are provided by mineral physics experiments coupled with dynamic considerations. On the basis of experimental determinations of the wave velocities in crystalline (Mg_{0.16}Fe_{0.84})O at megabar pressures (Wicks et al., 2010) and geodynamic simulations of this chemically distinct layer on top of the CMB (Bower et al., 2011), one can determine a percentage of iron-rich (Mg,Fe)O with an associated shape and velocity reduction, at a given temperature. As in Fig. 1C, a stable chemically distinct layer can be formed as a mechanical mixture of PREM-like silicates and a small volume of iron-rich (Mg,Fe)O. Ranges for relief and aspect ratio indicate variation due

* Correspondence to: University of Southern California, Department of Earth Sciences, ZHS, 3651 Trousdale Pkwy, Los Angeles, CA 90089, USA.
Tel.: +1 213 740 5842.

E-mail addresses: daoyuans@usc.edu (D. Sun), helm@gps.caltech.edu (D.V. Helmberger), jackson@gps.caltech.edu (J.M. Jackson), clay@gps.caltech.edu (R.W. Clayton), dan@caltech.edu (D.J. Bower).

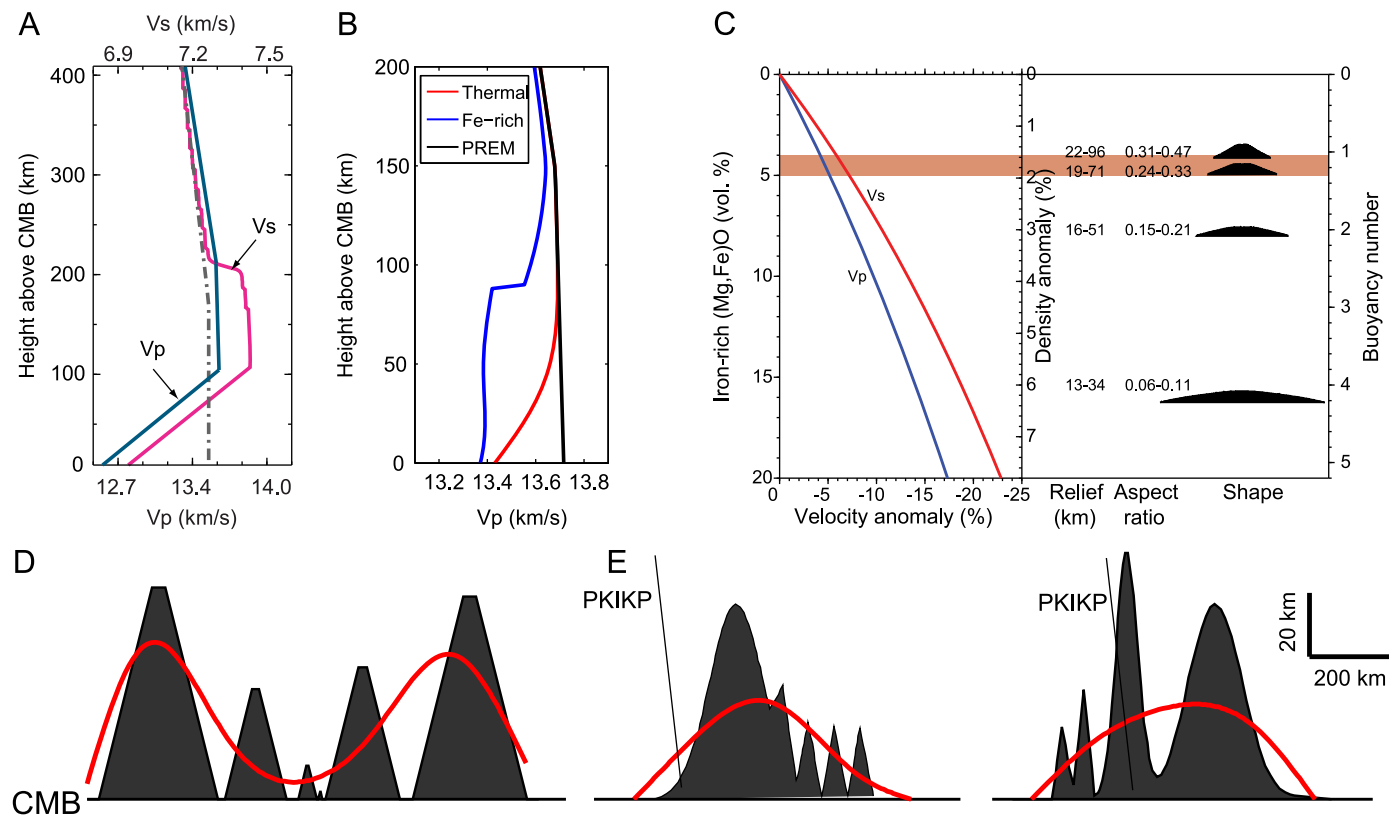


Fig. 1. Selection of reported structures on the core–mantle boundary (CMB). (A) Proposed prediction of phase boundary height above the CMB with a Clapeyron slope of 9 MPa/K for a proposed post-perovskite layer (Sun and Helmberger, 2008). (B) Proposed vertical velocity profiles near the CMB for a pure thermal vs. a distinct chemical layer. If the region just above the CMB is only a thermal boundary layer, we expect a concave upward morphology of the layer (red). (C) Display of wavespeed reductions (relative to PREM) and morphology of a chemically distinct layer formed as a mechanical mixture of PREM-like silicates and a small volume of iron-rich (Mg,Fe)O at $P=125$ GPa and $T=3500$ K. The orange shaded area indicates the possible ranges preferred by this report. (D) The dynamic modeling of such chemical heterogeneity suggests a complicated distribution of relatively sharp features assuming small volumes of iron-rich oxide, perhaps gardens of assorted shapes as displayed in (D); such distributions have been proposed by Wen and Helmberger (1998) as given in (E).

to initial volume of material (Bower et al., 2011). For a CMB temperature of ~ 3500 K, which falls within the loosely constrained range of 2800–4300 K (Lay et al., 2008), we make the following observations. Observed V_p values of ~ 13.00 km/s (-5% from PREM) correspond to 5 vol% of iron-rich (Mg,Fe)O mechanically mixed with co-existing pyrolytic-like silicates. The associated V_s reduction is 7.2% and the dynamically-stabilized structure is tent-like with ~ 78 –248 km widths. For a structure containing ~ 15 vol% of iron-rich (Mg,Fe)O, the V_p reductions would be 14% (relative to PREM) and the shape would be more dome-like, with widths ranging from ~ 120 to 600 km (Bower et al., 2011). In short, if iron-rich (Mg,Fe)O-bearing structures exist at the CMB, how do we detect them?

These results suggest a number of possible approaches for mapping such structures. If the velocity reductions are large, the structures are expected to be flat because of the high density of iron-rich (Mg,Fe)O (large buoyancy number in Fig. 1C). Such structures would be relatively easy to detect as precursors to P_cP , S_cS , and S_cP . There does not appear to be much support for such observations except in a few locations (Mori and Helmberger, 1995; Rost et al., 2010a, 2010b, 2005). In contrast, smaller reductions have high aspect ratios and have shapes capable of scattering short-period PKP phases. Precursors to PKIKP have been detected nearly everywhere (Hedlin and Shearer, 2000) and can be reasonably modeled with a garden of small-scale triangles sitting on the CMB (Wen, 2000; Wen and Helmberger, 1998) (Fig. 1E). We have smoothed the structure to display the type of features resolvable from modeling the SKS bifurcation presented in this report. In short, perhaps the CMB is covered

by gardens of high relief shapes (Fig. 1D) at some particular locations as suggested by strong scatter in differential PKP waveform variations (Sun et al., 2007).

2. SKS waveform modeling

As in most high-resolution techniques, one searches for a differential measure that focuses on the region of interest. It appears that the SKKS–SKS residuals and the bifurcation of SKS as observed by the massive USArray are ideal (Fig. 2). The SKS phase starts to become complicated near 107 – 109° where the S – P transmission coefficient at the CMB drops to zero and most of the energy is converted into a diffracted P -wave traveling horizontally in D' depending on local velocities. If the velocity increases above the CMB, the diffracted P energy is refracted back into the core and becomes the phase SP_dKS (diffraction at source side) and SKP_dS (diffraction at receiver side), called SKS_d in combination which are observed. The stronger this velocity gradient the stronger the SKS disruption near this bifurcation region (110°). Strongly disturbed waveforms at this range have been explained by inserting a ULVZ near the bifurcation point (Garnero and Helmberger, 1995, 1996, 1998; Helmberger et al., 1996; Rondenay et al., 2010; Thorne and Garnero, 2004).

The density of seismic ray paths used here (Fig. S1) allows stacking with exceptional coherency between samples as displayed in record section (Fig. 2B). At the distance range 111 – 114° , a model with a single-sided low velocity layer at one end and PREM on the other end (Helmberger et al., 1996) predicts the stacked data quite well. At large distance ($> 115^\circ$), the stacked data appear more

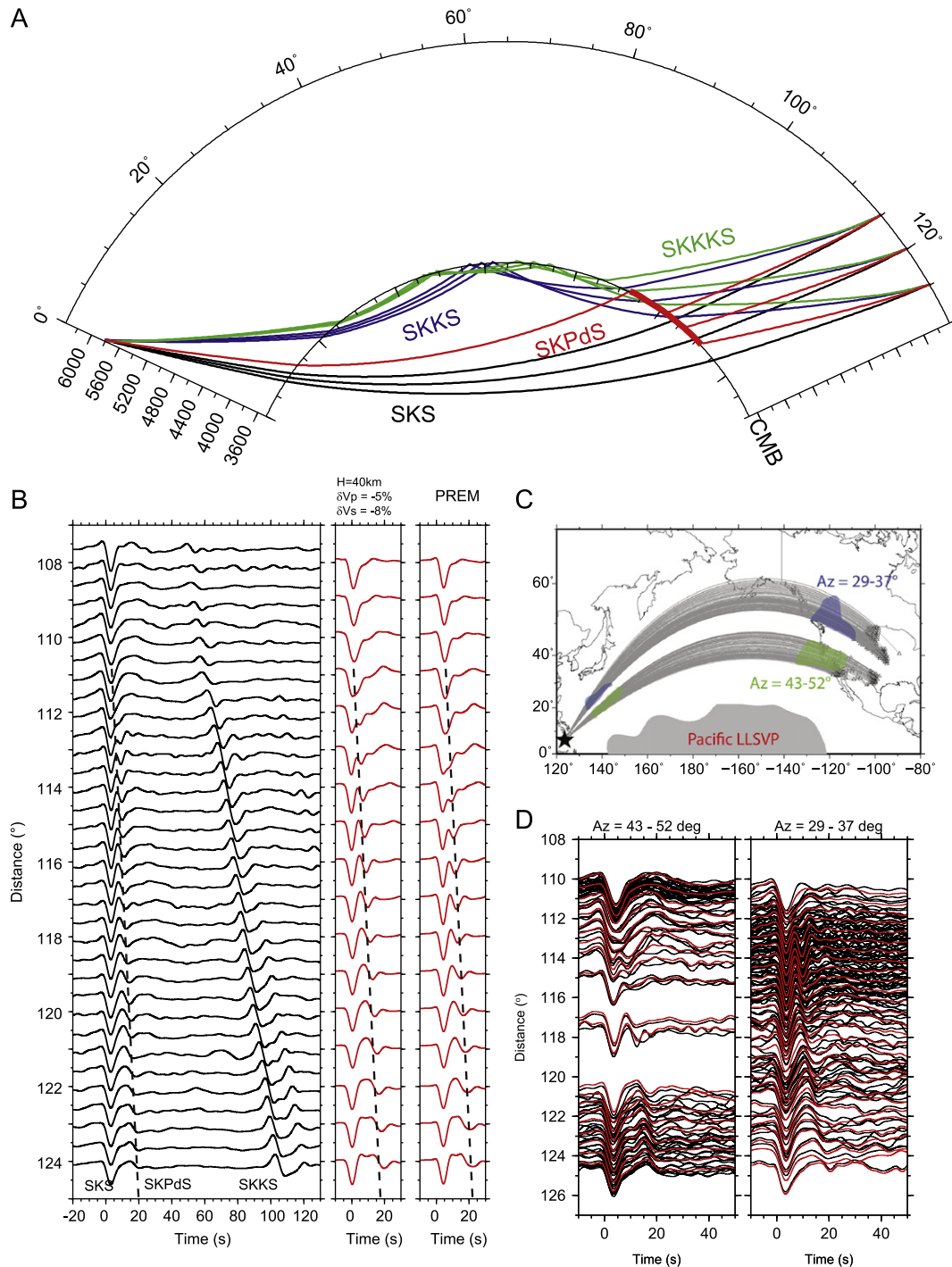


Fig. 2. Waveform observations from USArray along with some processing for a deep earthquake beneath the Philippines (20100724 in Table 1). The data are filtered with a bandpass filter (5–50 s). In (A), we display the stacked data (over 0.5° distance intervals) and aligned on SKS. When the data is viewed along different azimuths as in (C), we observe strong variation with corresponding stacks (red traces) given in (D). The strength of SKS_d is significantly stronger at ranges 112–115° at the smaller azimuths as is easily measured by the multiple-pathing detector (MPD) (red) in Fig. S2. (For interpretation of the references to color in this figure legend, the reader is referred to the web version of this article.)

PREM-like. A closer examination of the individual waveform data displays regional variation for two different azimuths (43–52° and 29–37°) as displayed in Fig. 2C and D.

Starting at about 112°, we can accurately measure the differential times between SKS_d and SKS with a multi-pathing analysis (Fig. S2). Because these two ray paths are nearly identical in the mantle and sample the 1-D liquid outer core (Fig. S1A), their differential behavior provides a direct measure of lateral variation

Table 1
Earthquakes used in this study.

Event	Date	Latitude (deg.)	Longitude (deg.)	Depth (km)
A	20100724	6.22	123.52	553
B	20100729	6.53	123.25	627
C	20091007	4.08	122.37	574

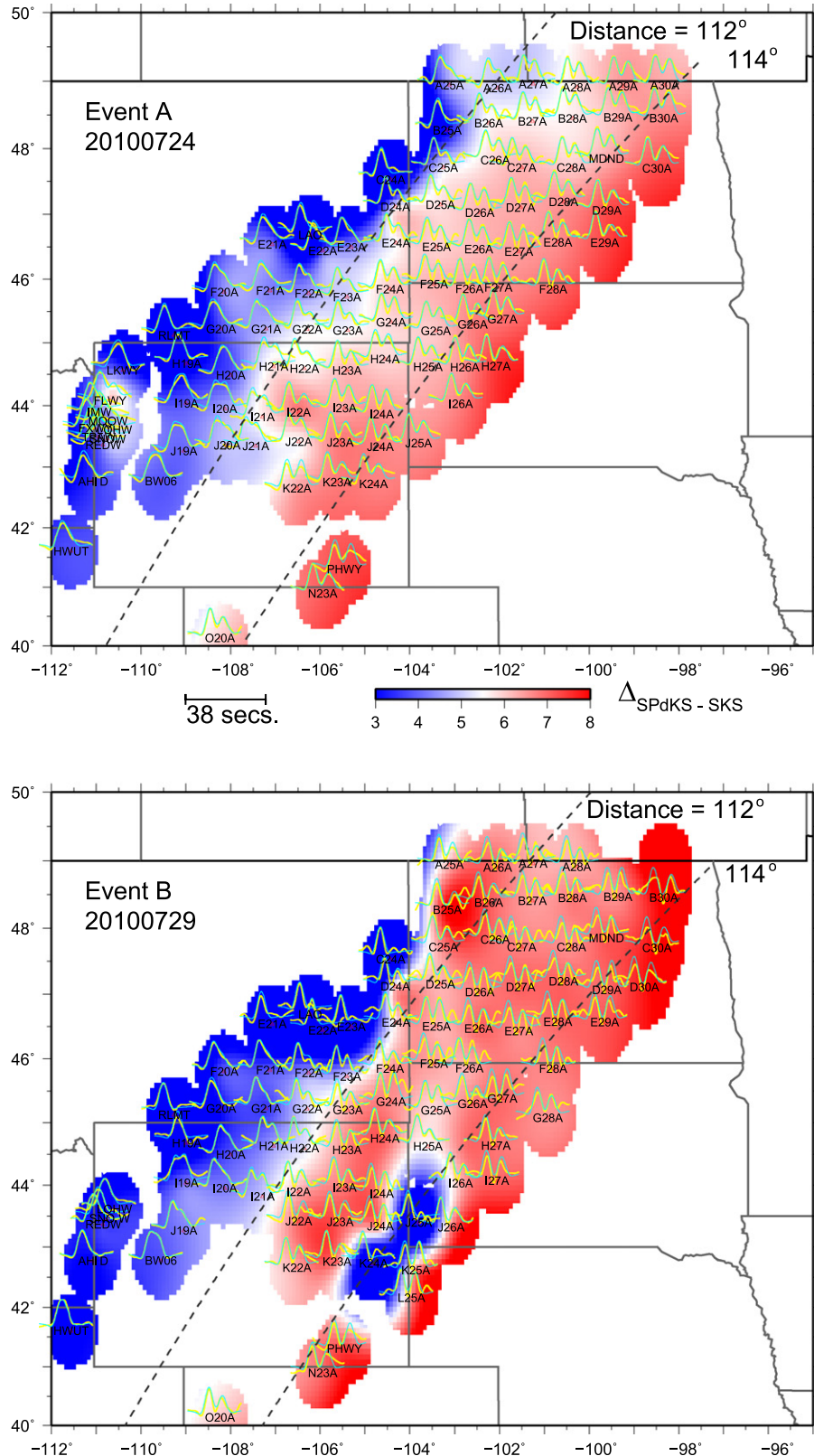


Fig. 3. The $\Delta T_{\text{SKS}_d - \text{SKS}}$ patterns together with the SKS+SKS_d waveform records for two events beneath the Philippines. The yellow traces are data records and cyan are MPD output. Although the event locations are similar, the patterns are slightly different. Especially for stations K24A and J25A, the SKS_d arrivals for 20100729 event (bottom) have much smaller amplitude than those in 20100724 event (top). The dash lines indicate the predicted wave-front for a 1D (PREM) model. (For interpretation of the references to color in this figure legend, the reader is referred to the web version of this article.)

over the short SKS_d segment. We have included two other events (Table 1) to show the expected shift in the pattern because of a small change in the source location. Thus, we can display the

pattern of delays at the recording sites as in Fig. 3. Indeed, neighboring events produce similar patterns except for some rather abrupt small-scale features. Note in Fig. 3, both events

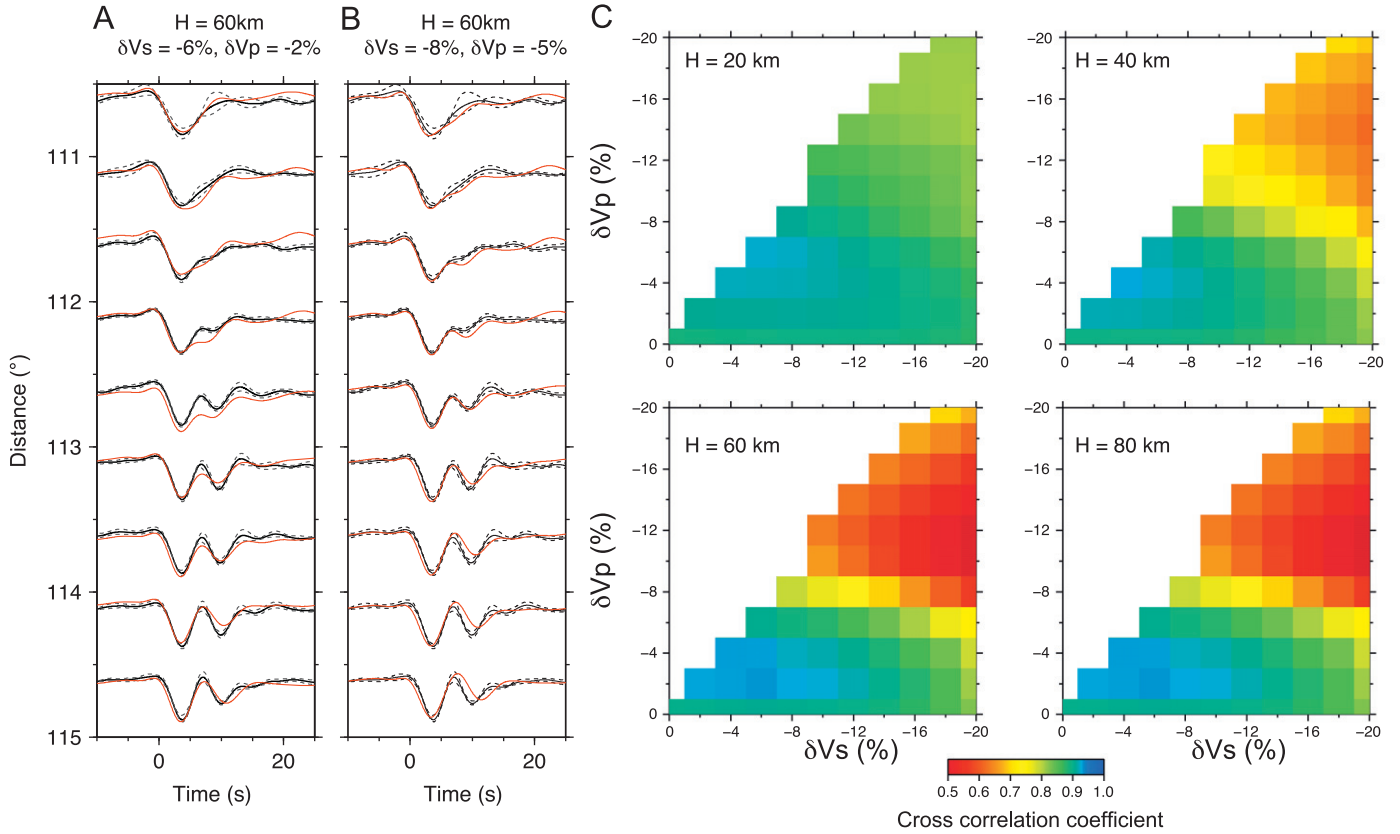


Fig. 4. SKS_d waveform inversion processing. In (A), we display data stacks from the Azi 29–37° interval (black solid traces with dash traces indicating the 95% confidence limits). The red traces are the best fitting synthetics (highest cross-correlations) assuming fixed $\delta V_p = -2\%$ and $\delta V_s = -6\%$ and searching for H . The same procedure is given in (B) but assuming $\delta V_p = -5\%$ and $\delta V_s = -8\%$. The complete set of trade-offs for this data (29–37°) is given in (C) with different H 's showing the non-uniqueness of this inversion. Note that large drops in velocity do not fit unless the H 's become very small where the waveform data is at noise-level. (For interpretation of the references to color in this figure legend, the reader is referred to the web version of this article.)

display a stronger and delayed SKS_d moving northward along the 112° azimuthal contour whereas at larger distance (114°), a still smaller-scale feature occurs in the 20100729 event (blue zone). In short, many individual records display complex waveforms which could be easily caused by site-responses and upper mantle features (Sun and Helmberger, 2011). However, most of the stations are now situated in the Great Plains and probably free of such tectonic features. Thus, we will attribute these features at the CMB where we will conduct some smoothing to highlight the main features at the CMB, which can be provided by localized stacking.

In Fig. 4, we take a closer look at the most anomalous waveforms (Azi=29–37°) for event A where the data have been stacked over a half degree interval in distance. A bootstrap-resampling algorithm was applied to evaluate the 95% confidence level where 300 random samples were used (Efron and Tibshirani, 1986). These waveforms when stacked are relatively simple and can be modeled by inserting a slow layer either at the source-side or receiver-side as proposed by Helmberger et al. (1996). In particular, we assume a flat layer thickness (H) with various values of δV_p and δV_s and generate a Green's function library. Every record is matched from the library and assembled in goodness-of-fit diagrams for H 's ranging from 0 to 100 km, in steps of 5 km. Synthetic seismograms with H less than 10 km are quite similar to those generated from PREM with these small velocity drops. Although the velocity drops cannot be well resolved, $\delta V_s = -8\%$ and $\delta V_p = -5\%$, fit the most anomalous recordings in the azimuth of 29–37° window over the 111–113° range. Note that here we explored the complete trade-off between δV_p , δV_s and H . Indeed, every record can be fit well with cross-correlations coefficients

larger than 0.9. The results are displayed in Fig. 4. At larger ranges, SKS_d is late for this model (Fig. 4B) and the lower δV (Fig. 4A) fits better. Thus, the goodness-of-fit estimates, based on cross-correlations, favor the lower δV solution for the whole distance range. Note at $H = 10$ km, almost any δV value works because the synthetics look PREM-like (Fig. 4C). Hence, a more tractable inversion is to fix the δV ratio and determine a H_i for every station. Examples of such fits are given in Fig. S4A for $\delta V_s = -6\%$ and $\delta V_p = -2\%$, and in Fig. S4B for $\delta V_s = -8\%$ and $\delta V_p = -5\%$. Thicknesses range from 5 to 100 km. The H_i value for each station is associated with a point on the CMB (projected along the ray path) at the midpoint of the P_d segment which is then used to construct maps. It appears that modeling stacked data produces the best fits as displayed in Fig. 5, essentially a 2D section through the data. Here, each stacked trace is modeled with a specific thickness and smoothed to produce the 2D structure. We also attempted to model all the individual records to generate a 3D structure. The three events produce similar patterns (Fig. S5) but with some difference. These estimates, roughly 1200 values, have been summed and smoothed to generate a 3D image (Fig. 6). To validate our results, we generated 2D synthetics along cross-sections AA' and BB' displayed in Fig. 6C, see Fig. S6A–C for details of this simulation. Along cross-section AA', the model predicts the strong SKS_d arrivals at smaller azimuth, especially at distance 112–114°. Although it is difficult to obtain a perfect match for every individual record, the topographic maps in Fig. 6 provide a reasonable image of the CMB and agree with the earlier MPD mapping. Only high quality MPD fits, with cross-correlations coefficients greater than 0.9, were used in constructing Fig. 6D. Two particularly slow regions (black dashed circles) are located beneath Nevada and British Columbia with smaller features beneath

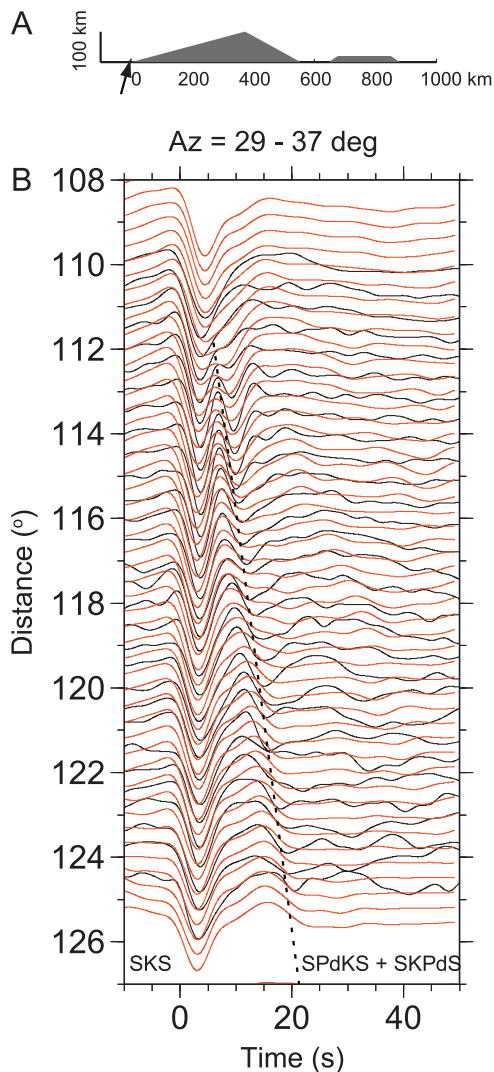


Fig. 5. The height inversion for stacked data along azimuth 29–37°. We cross-correlated every stacked data with one-side low velocity layer synthetics generated from GRT method to obtain the H 's along the profile. Then H 's are projected to CMB to generate the low velocity structure as in (A). In the layer: $\delta V_s = -8\%$, $\delta V_p = -5\%$. (B) Display of 2D synthetics (red) for the model in (A) with data (black). (For interpretation of the references to color in this figure legend, the reader is referred to the web version of this article.)

Oregon and a path towards the northeast. These same features are apparent in the thickness inversion with the two circles centered on the two highest hills. We have indicated the position of the strong local anomaly discussed earlier in Fig. 3, station results for J25A as an example. Note that this location is near the edge of the hill and difficult to model with our simple approach. A 3D simulation is given in Fig. S6C which appears similar to the 2D results displayed in Fig. 6C. A similar simulation for the source-side does not fit as well (Fig. S7) and can be understood in terms of the relatively large Fresnel sizes for these small δV values relative to ULVZ's (Fig. S8).

3. Validation

It is challenging to validate this model because most methods are less sensitive to the bottom most structure as discussed earlier. For example, one might think that the separation between SKKS–SKS travel times would be diagnostic. But even though these paths are similar in the upper mantle, they deviate enough

in the lower mantle to produce significant differences across this relatively small region. A few examples of SKS and SKKS CMB entry and exit points are denoted in Fig. 7A and B respectively, where the positions of events along the azimuths of 35° and 50° are displayed. The data is plotted in Fig. 7C for event A where the differential times cross near 118° with the separation increasing at larger azimuths. This feature occurs for all three events as given in Fig. S10 and can be seen in the stacked data sets as well (Fig. 8). Note that the SKKS–SKS arrivals at the distance 112–116° are closer together than at smaller azimuths (green). This trend reverses at larger distances. This feature is apparent for all three events which implies a lower mantle large scale variation. Indeed, the tomographic images can predict some of this trend when enhanced as displayed in Fig. 7C. The cross-over in distance occurs near 118° but actually changes significantly between the events (Fig. S10). Note that the two 2010 events are nearly collocated, especially at the larger azimuth. Along these paths, the travel time differentials for the two events agree quite well but differ a bit at smaller azimuths where the entry points are offset by less than 100 km. The 2009 event is quite distinct and samples a slightly different area (Fig. S1). Since SKKS paths are sampling the same regions as SKS_d, one would expect such a correspondence, and argues for the smooth 3D image presented in Fig. 6. In short, there is significant remaining scatter which appears to be mostly related to SKS when the stacking is aligned on SKKS (Fig. 8).

Still an even finer differential measure is between SKKS and SKKKS. As displayed in Fig. 2A, these phases cross the CMB within 100 km in distance at the source side, but spread out on the receiver side. Note that the SKS_d samples this zone both in distance and azimuth. An enlarged plot of the ray paths is given in Fig. 8A for the azimuth 29–37° sampling the most anomalous hill presented as a triangle. Note that SKKKS encounters the slow structure between 121° and 125° while the SKKS phase is clear of any structure. Thus, we would expect there to be a small timing delay between these two phases in this range. In contrast, the corridor with azimuth 43–60° does not have such a significant structure. Waveform data from these two corridors are presented in Fig. 9A. Although there is considerable scatter, there is a tendency for the separation between SKKS and SKKKS for azimuth 29–37° (green traces) to be greater by 1–2 s, which is consistent with the synthetic predictions given on the right in Fig. 9B. Unfortunately, this strongest hill feature is near the edge of the coverage and other event-station pairs are needed to better resolve the 3D-shape. Nevertheless, our data is at least self-consistent, where the position of anomalous SKP_dS samples agrees with the SKKS–SKKKS delays.

4. Discussion and summary

The SKS_d analysis presented above indicates that there is substantial evidence for lateral variation along the CMB boundary in a region devoid of ULVZ's (Rost et al., 2010b). In most global tomography models, our sampled regions are dominated by high velocity structures in the lowermost mantle. Ren et al. (2007) provide a model with low shear velocity lowermost mantle beneath western US and Canada, which overlapped with our results. In addition, the strong Sdiff arrivals in Figs. 2B and 8B also suggest possible low velocity layer along the Sdiff path but out of our resolution for the SKS_d phase. While the MPD simulations clearly show systematic variation, inverting these features for earth structure proves problematic for several reasons. First, there is the issue of where-is-it, source-side vs. receiver-side, or both. Secondly, there are strong trade-offs involving H (thickness) and between drops of V_p vs. V_s . Thirdly, if the H goes to zero, we need to locate these edges which creates still more parameters (i.e.,

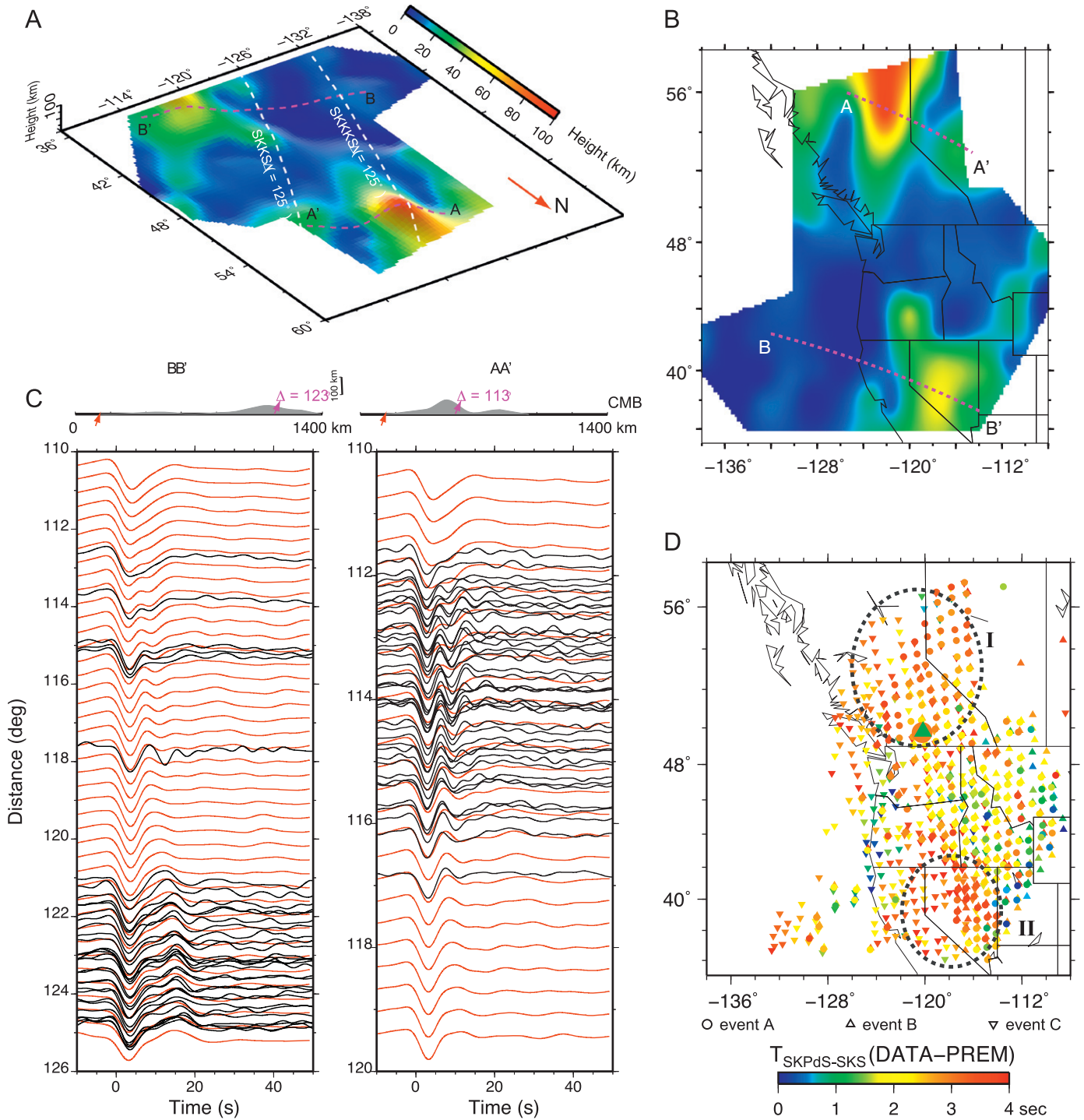


Fig. 6. Inversion results at long wavelengths. A 3D image of a laterally varying layer with average $\delta V_s = -8\%$ and $\delta V_p = -5\%$ is presented in (A) and map-view in (B). The two white lines indicate where the SKKS and SKKKS samples the CMB for a distance of 125° . Note the SKKKS samples the hill structure at smaller azimuth. The comparison between the original data (black) and 2D FD synthetics (red) along azimuths sampling profile AA' and BB' in Fig. 4C. The data along corridors with 2° width of AA' and BB' are plotted. Two-D structural sections are displayed on top. Red arrows indicate the critical distance for SKS at CMB. Magenta arrows indicate the core exit points of SKS_d for different distances. (D) Displays measured differential times between SKS_d and SKS for all three events by MPD projected to the CMB. Note that the circled regions I and II (large differential times) coincide with the hill structures in (B). Station J25A with very different differential times for events A and B as in Fig. 3 is highlighted with enlarged symbols. (For interpretation of the references to color in this figure legend, the reader is referred to the web version of this article.)

Rondenay et al., 2010). We have circumvented these issues by simply assuming that this layer exists everywhere although we allow it to be negligibly thin, an approach followed in dynamic modeling (i.e., McNamara et al., 2010). By constraining the velocity drops in V_p and V_s using existing experimental results on iron-rich oxide (Wicks et al. 2010), we developed a rolling-hills like structure consistent with our observations. Note that

structures along AA' and BB' in Fig. 6 have the aspect ratios (relief/half-width) of 0.5 and 0.2, respectively, suggesting that the material inside is ~ 1.5 – 2% denser than the surrounding material and contains ~ 4 – 5 vol% iron-rich (Mg,Fe)O (Fig. 1C). We note that the addition of iron into perovskite produces a noticeably denser assemblage that is more dome-like, with effectively little change in overall wave velocities (Bower et al. 2011). If an iron-rich

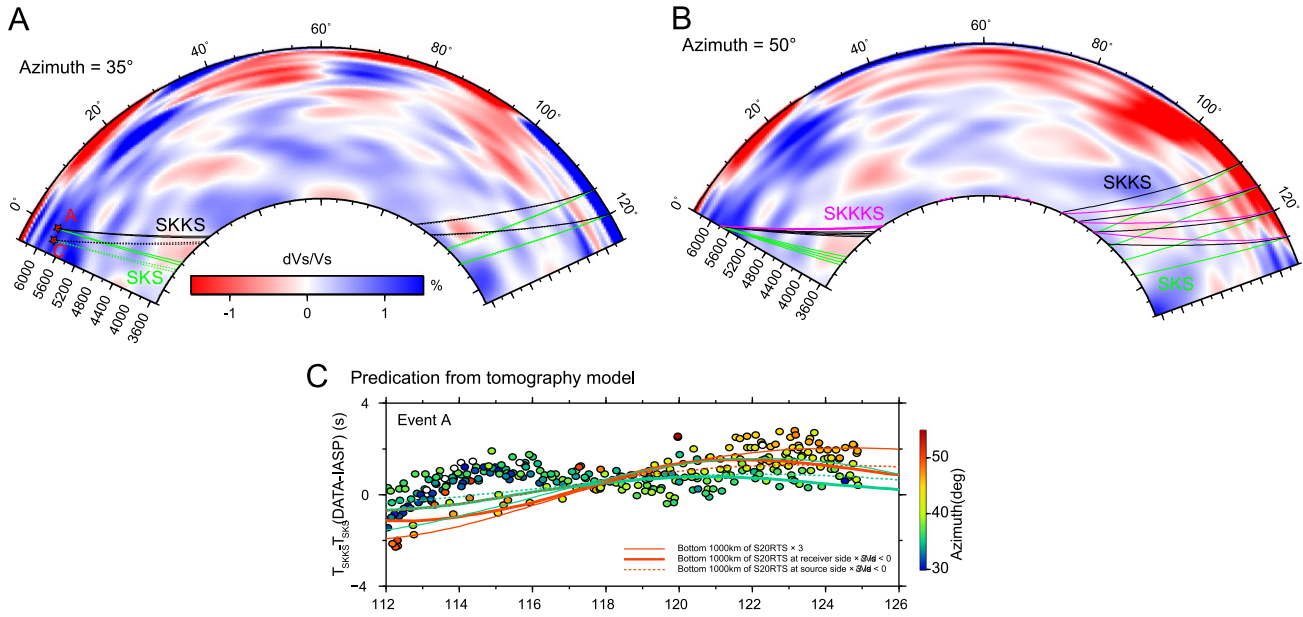


Fig. 7. Complexity in SKKS–SKS differential travel times. Cross-sections from S20RTS (Ritsema et al., 1999, 2004) at azimuths 35° (A) and 50° (B) contain the ray-paths for the three main phases; SKS (black), SKKS (red) and SKKS (green). The SKKS–SKS travel time residuals are given in (C) for event A. The tomographic predictions after inflation by multiplying the tomography by a constant factor, which is used to sharpen the typical smearing tomography images (Sun and Helmberger, 2011), are included. (For interpretation of the references to color in this figure legend, the reader is referred to the web version of this article.)

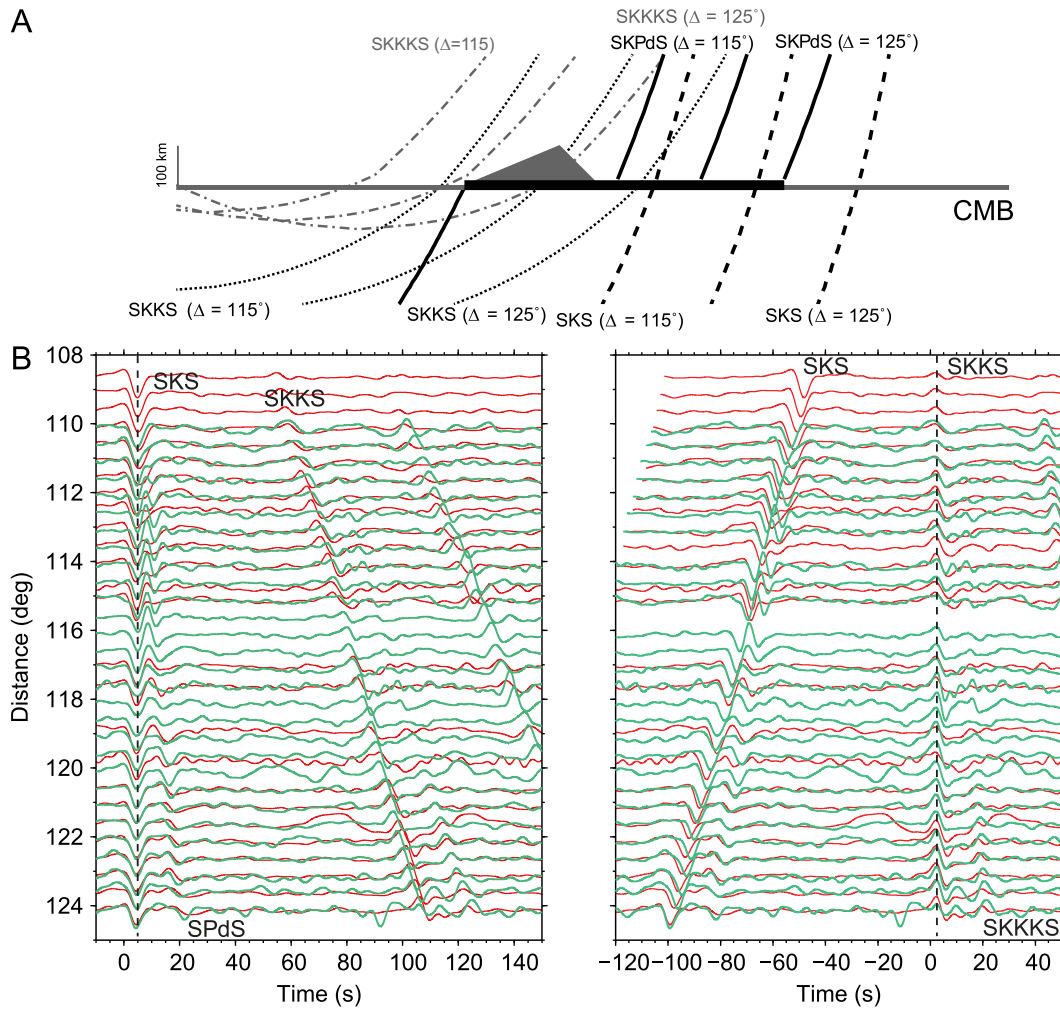


Fig. 8. The ray-paths for the four phases sampling the receiver-side structure is displayed in A; SKS (heavy-dashed), SKS_d (solid), SKKS (dotted), and SKKS (dotted-dashed). Again the stacked data for event A in the two azimuthal bins are displayed; 29–37° (green) and 43–60° (red). Note that SKKS and SKS_d sample the same region and provide better timing alignment than SKS and SKS_d at the larger distances. (For interpretation of the references to color in this figure legend, the reader is referred to the web version of this article.)

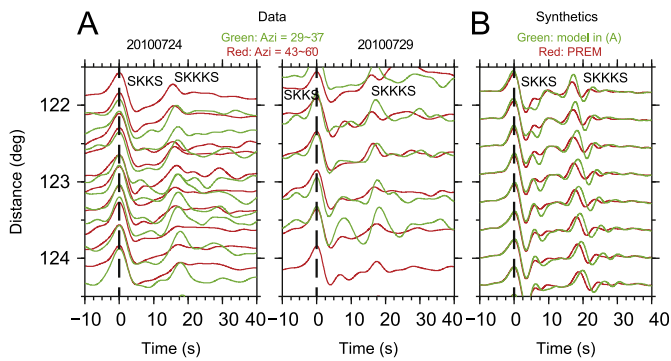


Fig. 9. Comparison of observed SKKS-SKKKS with synthetic predictions. The stacked waveforms for events A and B are again plotted in the azimuthal bins (A). Note that the SKKKS (green) traces are slightly delayed (1–2 s) and enhanced. This feature is predicted from the model as displayed in (B), although the data is noisy. (For interpretation of the references to color in this figure legend, the reader is referred to the web version of this article.)

post-perovskite assemblage is present (Mao et al., 2006), the velocities cannot be matched by seismic observations in this region and the resulting structure would be effectively flat over the CMB. Provided the existing experimental results on candidate solid phases and dynamic modeling, we find that the best match to our seismic observations of wave speeds and topography is a silicate-rich assemblage bearing ~5 vol% iron-rich (Mg,Fe)O. Our observation suggests that this region is therefore chemically heterogeneous.

Formation of an iron-rich oxide-bearing structure has been discussed previously (e.g., Knittle and Jeanloz, 1991). In partitioning studies involving mantle materials and average mantle compositions, (Mg,Fe)O has been shown to be the favored sink for iron (Sakai et al., 2010). Obtaining high iron concentrations on the mantle side of the CMB may involve reactions with the liquid iron-dominant outer core (Knittle and Jeanloz, 1991), fractional crystallization of a magma ocean (Labrosse et al., 2007), partial melting (Williams and Garnero, 1996), mechanical mixing (Kanda and Stevenson, 2006), and/or a combination of the above scenarios. Reactions involving the outer core are more likely to be stabilized as thin layers, less than ~10's km high. Whereas, thicker, dynamically stabilized structures, resting on the CMB could more likely form as residuals from global melting events in Earth's early history (Labrosse et al., 2007). Chemical interactions between the core and the mantle (Buffett and Seagle, 2010) or light elements released from the crystallization of the inner core (Helffrich and Kaneshima, 2010) may form a stratified layer at the top of the core, which may produce another possible explanation, especially for the SmKS travel times (Garnero et al., 1993; Helffrich and Kaneshima, 2010). A global study is still required to make further evaluations about the effects of core side or mantle side structures on SKSd and SmKS.

In conclusion, we have presented the analysis of a large dataset consisting of the phase SKP_dS sampling beneath Western North America. This region is thought to be dominated by old-slab material and devoid of ULVZ's. Our observations suggest that a low-velocity zone exists varying in thickness up to 100 km high. Although our modeling results are admittedly non-unique, we put forward a model defendable from a self-consistent interpretation of data involving a multi-disciplinary approach.

Acknowledgments

The authors would like to thank the Editor Peter Shearer and two anonymous reviewers for their constructive comments. We thank J.K. Wicks and M. Gurnis for stimulating conversations and

a constructive review by Alex Song. Data were provided by IRIS data centers and Earthscope US Array. This work was supported by NSF CSEDI EAR-0855815. D. Sun is supported by a Carnegie fellowship at the Department of Terrestrial Magnetism, Carnegie Institution of Washington.

Appendix A. Supplementary material

Supplementary data associated with this article can be found in the online version at <http://dx.doi.org/10.1016/j.epsl.2012.10.027>.

References

- Bower, D.J., Wicks, J.K., Gurnis, M., Jackson, J.M., 2011. A geodynamic and mineral physics model of a solid-state ultralow-velocity zone. *Earth Planet. Sci. Lett.* 303, 193–202.
- Buffett, B.A., Seagle, C.T., 2010a. Stratification of the top of the core due to chemical interactions with the mantle. *J. Geophys. Res.* 115, B04407, <http://dx.doi.org/10.1029/2009jb006751>.
- Efron, B., Tibshirani, R., 1986. Bootstrap methods for standard errors, confidence intervals, and other measures of statistical accuracy. *Stat. Sci.* 1, 54–75.
- Garnero, E.J., Helmberger, D.V., 1995. A very slow basal layer underlying large-scale low-velocity anomalies in the lower mantle beneath the Pacific—evidence from core phases. *Phys. Earth Planet. Inter.* 91, 161–176.
- Garnero, E.J., Helmberger, D.V., 1996. Seismic detection of a thin laterally varying boundary layer at the base of the mantle beneath the central-Pacific. *Geophys. Res. Lett.* 23, 977–980.
- Garnero, E.J., Helmberger, D.V., 1998. Further structural constraints and uncertainties of a thin laterally varying ultralow-velocity layer at the base of the mantle. *J. Geophys. Res.* 103, 12495–12509.
- Garnero, E.J., Helmberger, D.V., Grand, S.P., 1993. Constraining outermost core velocity with SmKS waves. *Geophys. Res. Lett.* 20, 2463–2466.
- Hedlin, M.A.H., Shearer, M., 2000. An analysis of large-scale variations in small-scale mantle heterogeneity using Global Seismographic Network recordings of precursors to PKP. *J. Geophys. Res.* 105, 13655–13673.
- Helffrich, G., Kaneshima, S., 2010. Outer-core compositional stratification from observed core wave speed profiles. *Nature* 468 (7325), 807–810.
- Helmberger, D., Lay, T., Ni, S., Gurnis, M., 2005. Deep mantle structure and the postperovskite phase transition. *Proc. Natl. Acad. Sci.* 102, 17257–17263.
- Helmberger, D.V., Garnero, E.J., Ding, X., 1996. Modeling two-dimensional structure at the core–mantle boundary. *J. Geophys. Res.* 101, 13963–13972.
- Helmberger, D.V., Wen, L., Ding, X., 1998. Seismic evidence that the source of the Iceland hotspot lies at the core–mantle boundary. *Nature* 396 (6708), 251–255.
- Hernlund, J.W., Tackley, J., 2007. Some dynamical consequences of partial melting in Earth's deep mantle. *Phys. Earth Planet. Inter.* 162, 149–163.
- Hernlund, J.W., Thomas, C., Tackley, J., 2005. A doubling of the post-perovskite phase boundary and structure of the Earth's lowermost mantle. *Nature* 434, 882–886.
- Hirose, K., 2006. Postperovskite phase transition and its geophysical implications. *Rev. Geophys.* 44, RG3001, <http://dx.doi.org/10.1029/2005RG000186>.
- Jeffreys, H., 1962. *The Earth, Its Origin, History and Physical Constitution*. Cambridge University Press, Cambridge.
- Kanda, R.V.S., Stevenson, D.J., 2006. Suction mechanism for iron entrapment into the lower mantle. *Geophys. Res. Lett.* 33, L02310, <http://dx.doi.org/10.1029/2005gl025009>.
- Knittle, E., Jeanloz, R., 1991. Earth's core–mantle boundary—results of experiments at high-pressures and temperatures. *Science* 251, 1438–1443.
- Labrosse, S., Hernlund, J.W., Coltice, N., 2007. A crystallizing dense magma ocean at the base of the Earth's mantle. *Nature* 450, 866–869.
- Lay, T., Garnero, E.J., 2011. Deep mantle seismic modeling and imaging. *Annu. Rev. Earth Planet. Sci.* 39, 91–123.
- Lay, T., Hernlund, J., Buffett, B.A., 2008. core–mantle boundary heat flow. *Nat. Geosci.* 1, 25–32.
- Mao, W.L., Mao, H.K., Sturhahn, W., Zhao, J.Y., Prakapenka, V.B., Meng, Y., Shu, J.F., Fei, Y.W., Hemley, R.J., 2006. Iron-rich post-perovskite and the origin of ultralow-velocity zones. *Science* 312, 564–565.
- Mao, W.L., Shen, G.Y., Prakapenka, V.B., Meng, Y., Campbell, A.J., Heinz, D.L., Shu, J.F., Hemley, R.J., Mao, H.K., 2004. Ferromagnesian postperovskite silicates in the D'' layer of the Earth. *Proc. Natl. Acad. Sci.* 101, 15867–15869.
- McNamara, A.K., Garnero, E.J., Rost, S., 2010. Tracking deep mantle reservoirs with ultra-low velocity zones. *Earth Planet. Sci. Lett.* 299, 1–9.
- Mori, J., Helmberger, D.V., 1995. Localized boundary-layer below the mid-Pacific velocity anomaly identified from a PcP precursor. *J. Geophys. Res.* 100, 20359–20365.
- Mosenfelder, J.L., Asimow, D., Ahrens, T.J., 2007. Thermodynamic properties of Mg₂SiO₄ liquid at ultra-high pressures from shock measurements to 200 GPa on forsterite and wadsleyite. *J. Geophys. Res.* 112, 13B06208, <http://dx.doi.org/10.1029/2006JB004364>.

- Murakami, M., Hirose, K., Kawamura, K., Sata, N., Ohishi, Y., 2004. Post-perovskite phase transition in MgSiO_3 . *Science* 304, 855–858.
- Oganov, A.R., Ono, S., 2004. Theoretical and experimental evidence for a post-perovskite phase of MgSiO_3 in Earth's D'' layer. *Nature* 430, 445–448.
- Ren, Y., Stutzmann, E., van der Hilst, R.D., Besse, J., 2007. Understanding seismic heterogeneities in the lower mantle beneath the Americas from seismic tomography and plate tectonic history. *J. Geophys. Res.* 112, B01302, <http://dx.doi.org/10.1029/2005JB004154>.
- Ritsema, J., van Heijst, H.J., Woodhouse, J.H., 1999. Complex shear wave velocity structure imaged beneath Africa and Iceland. *Science* 286, 1925–1928.
- Ritsema, J., van Heijst, H.J., Woodhouse, J.H., 2004. Global transition zone tomography. *J. Geophys. Res.* 109, B02302, <http://dx.doi.org/10.1029/2003jb002610>.
- Rondenay, S., Cormier, V.F., Van Ark, E.M., 2010. SKS and SPdKS sensitivity to two-dimensional ultralow-velocity zones. *J. Geophys. Res.* 115, B04311, <http://dx.doi.org/10.1029/2009jb006733>.
- Rost, S., Garnero, E.J., Stefan, W., 2010a. Thin and intermittent ultralow-velocity zones. *J. Geophys. Res.* 115, B06312, <http://dx.doi.org/10.1029/2009jb006981>.
- Rost, S., Garnero, E.J., Thorne, M.S., Hutko, A.R., 2010b. On the absence of an ultralow-velocity zone in the North Pacific. *J. Geophys. Res.* 115, B04312, <http://dx.doi.org/10.1029/2009jb006420>.
- Rost, S., Garnero, E.J., Williams, Q., Manga, M., 2005. Seismological constraints on a possible plume root at the core–mantle boundary. *Nature* 435, 666–669.
- Sakai, T., Ohtani, E., Terasaki, H., Miyahara, M., Nishijima, M., Hirao, N., Ohishi, Y., Sata, N., 2010. Fe–Mg partitioning between post-perovskite and ferroperricite in the lowermost mantle. *Phys. Chem. Miner.* 37, 487–496.
- Sidorin, I., Gurnis, M., Helmberger, D.V., 1999. Evidence for a ubiquitous seismic discontinuity at the base of the mantle. *Science* 286, 1326–1331.
- Sun, D., Helmberger, D., 2008. Lower mantle tomography and phase change mapping. *J. Geophys. Res.* 113, B10305, <http://dx.doi.org/10.1029/2007jb005289>.
- Sun, D., Helmberger, D., 2011. Upper-mantle structures beneath USArray derived from waveform complexity. *Geophys. J. Int.* 184, 416–438.
- Sun, X., Song, X., Zheng, S., Helmberger, D.V., 2007. Evidence for a chemical–thermal structure at base of mantle from sharp lateral P-wave variations beneath Central America. *Proc. Natl. Acad. Sci.* 104, 26–30.
- Thorne, M.S., Garnero, E.J., 2004. Inferences on ultralow-velocity zone structure from a global analysis of SPdKS waves. *J. Geophys. Res.* 109, B08301, <http://dx.doi.org/10.1029/2004jb003010>.
- van der Hilst, R.D., de Hoop, M.V., Wang, Shim, S.H., Ma, P., Tenorio, L., 2007. Seismostratigraphy and thermal structure of Earth's core–mantle boundary region. *Science* 315, 1813–1817.
- Wen, L.X., 2000. Intense seismic scattering near the Earth's core–mantle boundary beneath the Comoros hotspot. *Geophys. Res. Lett.* 27, 3627–3630.
- Wen, L.X., Helmberger, D.V., 1998. Ultra-low velocity zones near the core–mantle boundary from broadband PKP precursors. *Science* 279, 1701–1703.
- Wicks, J.K., Jackson, J.M., Sturhahn, W., 2010. Very low sound velocities in iron-rich (Mg, Fe)O: implications for the core–mantle boundary region. *Geophys. Res. Lett.* 37, L15304, <http://dx.doi.org/10.1029/2010GL043689>.
- Williams, Q., Garnero, E.J., 1996. Seismic evidence for partial melt at the base of Earth's mantle. *Science* 273, 1528–1530.